

Estimating Tropical Cyclone Integrated Kinetic Energy with the CYGNSS Satellite Constellation

MARY MORRIS AND CHRISTOPHER S. RUF

*Department of Climate and Space Sciences and Engineering, College of Engineering,
University of Michigan, Ann Arbor, Michigan*

(Manuscript received 9 May 2016, in final form 17 October 2016)

ABSTRACT

The Cyclone Global Navigation Satellite System (CYGNSS) constellation is designed to provide observations of surface wind speed in and near the inner core of tropical cyclones with high temporal resolution throughout the storm's life cycle. A method is developed for estimating tropical cyclone integrated kinetic energy (IKE) using CYGNSS observations. IKE is calculated for each geographically based quadrant out to an estimate of the 34-kt ($1 \text{ kt} = 0.51 \text{ m s}^{-1}$) wind radius. The CYGNSS-IKE estimator is tested and its performance is characterized using simulated CYGNSS observations with realistic measurement errors. CYGNSS-IKE performance improves for stronger, more organized storms and with increasing number of observations over the extent of the 34-kt radius. Known sampling information can be used for quality control. While CYGNSS-IKE is calculated for individual geographic quadrants, using a total-IKE—a sum over all quadrants—improves performance. CYGNSS-IKE should be of interest to operational and research meteorologists, insurance companies, and others interested in the destructive potential of tropical cyclones developing in data-sparse regions, which will now be covered by CYGNSS. The CYGNSS-IKE product will be available for the 2017 Atlantic Ocean hurricane season.

1. Introduction

a. Tropical cyclone intensity classifications and complications

Tropical cyclones (TCs) are routinely categorized according to the intensity of storm winds, as either the maximum sustained 1- or 10-min wind speed (V_{MAX}). Routinely used in the United States, the Saffir–Simpson hurricane wind scale (SSHWS) categorizes hurricanes with the 1-min sustained V_{MAX} (Saffir 1975; Simpson 1974). Using a single, intensity-related input often does not tell the whole story of the destructive potential of a TC. Both size and intensity matter.

The deficiencies of the SSHWS as a predictor of destructive potential have been acknowledged in numerous previous studies (e.g., Mahendran 1998; Kantha 2006; Powell and Reinhold 2007; Irish et al. 2008; Maclay et al. 2008). The limitations of SSHWS are most clearly shown by a comparison between the destruction from Hurricanes Katrina (2005) and Camille (1969) (Irish et al. 2008; Powell and Reinhold 2007). Hurricane Camille, with a

landfall intensity of 150 kt ($1 \text{ kt} = 0.51 \text{ m s}^{-1}$), maxing out the SSHWS at category 5, is now considered to be the second-most-intense hurricane in the United States record, surpassed only by the 1953 Labor Day hurricane (Kieper et al. 2016). Hurricane Katrina made landfall in the same area, but as a category-3 storm with an intensity of 110 kt (Knabb et al. 2005). Despite being two SSHWS classifications below Hurricane Camille, Hurricane Katrina was a much larger storm than Camille at landfall, which led to a significantly more destructive storm surge (Knabb et al. 2005; Irish et al. 2008).

The comparison of hurricanes Katrina and Camille highlights the need for a TC strength scale that depends on both the intensity of the winds and the size of the storm. First proposed by Powell and Reinhold (2007), integrated kinetic energy (IKE) can be used to supplement the SSHWS. IKE is defined here as

$$\text{IKE} = \int_{V/2} \frac{1}{2} \rho U^2 dV \quad (1)$$

where U , the surface wind speed, is integrated over a specified volume V of the storm, taking into account the air density ρ . IKE is considered to be a better measure of

Corresponding author e-mail: Mary Morris, marygm@umich.edu

the destructive potential of TCs than SSHWS because it quantifies both the spatial extent and the strength of the winds.

b. Previous IKE studies

Since first being introduced, several IKE-related products have been proposed. IKE is now included in the set of NOAA's Hurricane Research Division (HRD) Real-Time Hurricane Wind Analysis System (H*Wind) products (Powell et al. 1998; 2010). H*Wind IKE can be computed from H*Wind analyses that combine all available surface wind speed observations for storms in real time, as well as in poststorm reanalyses. H*Wind products have been recently commercialized, and current products are no longer publicly available; however, the legacy dataset, created when these products were supported through NOAA, is still publicly available. H*Wind products are heavily reliant on data availability—in particular, on observations collected from reconnaissance aircraft. The coverage and availability of H*Wind products is concentrated in the Atlantic Ocean and eastern Pacific Ocean basins.

In a study by Maclay et al. (2008), low-level IKE was calculated from flight-level aircraft reconnaissance data, and an experimental, multisatellite, IKE-based product developed from this work is now available from the NOAA/NESDIS/Center for Satellite Applications and Research (STAR)/Regional and Mesoscale Meteorology Branch (RAMMB) real-time TC data product page (NOAA/NESDIS/STAR/RAMMB 2016). Unlike the IKE product to be developed in this study, IKE is calculated over a 1-km depth and at 700 hPa, rather than over a 1-m depth at the surface level. Maclay et al. (2008) went to considerable lengths to categorize the 700-hPa IKE further by a simple 0–5 scale to create easier comparisons with the categorization employed by the SSHWS.

IKE metrics like the track IKE have been proposed as more useful analysis metrics for seasonal activity: Misra et al. (2013) followed up on this proposal. Additionally, work has been performed on the statistical predictability of IKE (Kozar and Misra 2014; Kozar 2015; Kozar et al. 2016).

c. Existing sensors for surface wind speed estimation

The spaceborne sensors and imagery that have supported the above IKE products (Maclay et al. 2008; Powell et al. 1998; 2010) include scatterometers; infrared, visible, and water vapor imagery; and microwave sounders. Scatterometers provide surface wind speed estimates but are limited to regions without heavy precipitation, saturate at high wind speeds, and are also known to have poor revisit time (Brennan et al. 2009;

Hennon et al. 2006). Infrared and visible imagery allow for the estimation of low-level winds by tracking cloud features (e.g., Dunion and Velden 2002; Holmlund et al. 2001; Velden et al. 1997, 2005). Generally, the feature-tracking methods will not work for low-level wind estimation if the low-level features being tracked are obscured by high cloud tops, for example, near the center of a tropical cyclone. It is also possible to estimate low-level wind parameters using infrared data, but these methods require an estimate of storm intensity (Kossin et al. 2007; Knaff et al. 2015; Mueller et al. 2006). Advanced Microwave Sounding Unit (AMSU) soundings can inform estimates of the two-dimensional midlevel wind field after solving the nonlinear balance equation. However, AMSU estimated winds are known to be poor near storm centers since the resolution of the product is limited, with 50–120-km footprints (Bessho et al. 2006). Low-level winds estimated through these methods will have to be adjusted to the surface (Knaff et al. 2011). All of these sensors have limited utility for estimating surface wind speed in the heavy-precipitation and high-cloud-shielded region of the TC eyewall. Additionally, the polar-orbiting sensors will have inadequate temporal sampling for the time scales typical of TC rapid intensification.

d. CYGNSS

The Cyclone Global Navigation Satellite System (CYGNSS) constellation of eight small satellites, launched on 15 December 2016, provides unique ocean surface wind speed observations in all precipitating conditions (Ruf et al. 2016). The mean and median revisit times for the constellation over the entire tropics are 7.2 and 2.8 h, respectively. The resolution of the wind speed product will be $25 \times 25 \text{ km}^2$ or better, with 2 m s^{-1} retrieval uncertainty for winds less than 20 m s^{-1} and 10% retrieval uncertainty for winds greater than 20 m s^{-1} . Given the ability to penetrate through the high precipitation of a TC eyewall to observe the highest surface wind speeds of TCs, and the rapid temporal sampling, CYGNSS is well suited to estimate IKE.

There are some challenges to overcome with this new observing system. Since CYGNSS operates in a bistatic radar type set up with GNSS transmitters, the sampling patterns are not analogous to the continuous-swath observations typical of other spaceborne wind sensing instruments. Instead, CYGNSS observes winds along a series of narrow tracks through the storm. Portions of the wind field between the tracks are not directly sampled and must be estimated as part of the IKE algorithm discussed in this paper. It should be noted that there are currently no plans for near-real-time ground processing of CYGNSS data. In the future, if the CYGNSS mission

successfully demonstrates the value of its data products, a transition to near-real-time operations is possible and the IKE data product could be available to operational agencies.

e. Objectives and overview

The main objectives of this study are to develop and characterize a CYGNSS-based IKE product for tropical storms and cyclones (CYGNSS-IKE). Section 2 describes the datasets used. Section 3 presents the CYGNSS-IKE algorithm concept and implementation. The subsequent sections address the characterization of the algorithm in three respects:

- 1) How well does CYGNSS-IKE perform?
- 2) How well can the confidence in CYGNSS-IKE be determined from CYGNSS data alone?
- 3) What are the dominant error contributors to CYGNSS-IKE?

2. Datasets

To test the CYGNSS-IKE algorithm prelaunch, a large set of simulated observations was created using the CYGNSS end-to-end-simulator (E2ES) (O'Brien 2014). The E2ES generates simulated CYGNSS level 2 wind speed data products from a time-evolving input wind field. It properly accounts for both the spatial and temporal peculiarities of the CYGNSS measurement technique by forward propagating the orbital trajectories of every satellite in the GPS and CYGNSS constellations and computing the location of the specular reflection point on Earth's surface as a function of time for every possible GPS-CYGNSS pair. The E2ES also properly accounts for the 25-km spatial resolution of the CYGNSS wind speed measurements by appropriately averaging the input wind field and for its measurement uncertainty by corrupting the input "truth" winds with noise that is statistically representative of the expected precision of the level 2 wind speed retrieval algorithm (Clarizia and Ruf 2016).

Simulated CYGNSS observations were generated using real-time wind field analyses produced by the operational version of the Hurricane Weather Research and Forecasting (HWRF) system (Tallapragada et al. 2013) for most Atlantic and west Pacific storms during the 2010 and 2011 hurricane seasons. HWRF wind fields were generated for 25 different storms every 3 h throughout their life cycles. Times during which the storm center was within 200 km of a major landmass were excluded from this study. This resulted in a total of 201 three-hour intervals in which CYGNSS observations were simulated from the HWRF "truth" wind

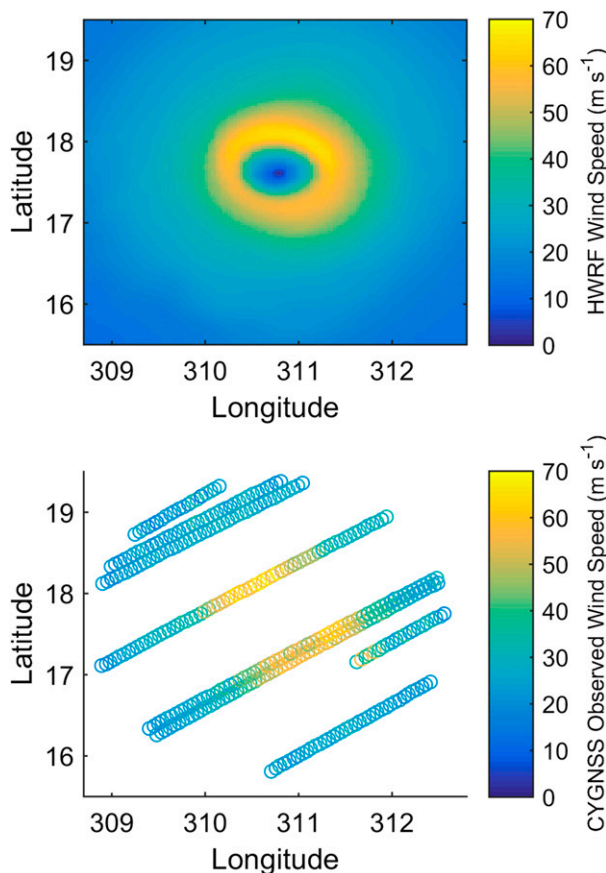


FIG. 1. (top) An example of an HWRf wind analysis for Hurricane Igor, 1200 UTC 13 Sep 2010. (bottom) Simulated CYGNSS observations that correspond to the HWRf wind analysis within 200 km of the storm center for the time period 1200–1500 UTC 13 Sep 2010.

fields. An example of an HWRf input wind field for one of these 3-h periods, together with the simulated observations by CYGNSS that would have been made over that interval of time, within 200 km of the storm center, is shown in Fig. 1. A summary of all of the storms used in this study is given in Table 1.

3. Methodology

Determination of the IKE requires that the integral expression in Eq. (1) be evaluated. This, in turn, requires that the wind speed be known (or estimated) at every location within the vicinity of the storm bounded by the limits of integration. In the case of CYGNSS, actual measurements of the wind occur along a series of narrow tracks through the storm, as illustrated in Fig. 1. Values of the wind speed in between the actual observations, which are needed to compute the IKE, are estimated by fitting a parametric model of the wind structure to the observations and then using the model to interpolate between the observations.

TABLE 1. A summary of all of the storms used in this study, with the storm name, the number of cases for that particular storm, the maximum wind speed (V_{MAX}) of the cases considered, the storm center latitude and longitude of the storm at the point in time corresponding to the V_{MAX} case, and the month and year time period for each storm.

Storm name	No. of storm test cases	V_{MAX} ($m s^{-1}$)	Storm center lat ($^{\circ}N$)	Storm center lon ($^{\circ}E$)	Storm test case month(s)	Storm test case year
Colin	7	27	27.4	293.0	Aug	2010
Danielle	13	54	26.8	300.3	Aug	2010
Earl	5	23	15.0	324.8	Aug	2010
Estelle	8	27	17.3	250.8	Aug	2010
Fiona	4	29	24.3	293.8	Aug-Sep	2010
Frank	2	40	17.6	250.6	Aug	2010
Gaston	8	16	17.4	304.5	Sep	2010
Igor	18	66	17.6	310.7	Sep	2010
Julia	11	59	17.7	327.8	Sep	2010
Matthew	1	20	14.0	282.3	Sep	2010
Ten	1	24	19.8	250.4	Sep	2010
Adrian	10	63	14.5	254.7	Jun	2011
Bret	3	24	29.8	284.0	Jul	2011
Calvin	3	36	16.7	250.9	Jul	2011
Dora	2	41	19.4	250.6	Jul	2011
Eugene	18	61	15.7	245.3	Jul-Aug	2011
Fernanda	14	28	14.6	217.3	Aug	2011
Gert	5	26	32.9	297.3	Aug	2011
Greg	9	36	18.5	248.6	Aug	2011
Hilary	13	59	17.1	250.6	Sep	2011
Irwin	2	22	15.2	240.9	Oct	2011
Katia	19	55	27.0	294.1	Aug-Sep	2011
Maria	6	33	33.7	293.1	Sep	2011
Ophelia	8	50	24.0	296.9	Sep	2011
Philippe	11	25	14.9	326.4	Sep	2011

To create an operationally relevant IKE product, IKE is integrated over each geographically based quadrant out to the 34-kt wind radius (R_{34}). If a storm is weaker than 34 kt, the R_{34} threshold is not attained, and IKE is not estimated. For the case of the true IKE, R_{34} is found directly from the fully sampled HWRF wind field that is integrated to get the IKE. For the case of the IKE retrieved from CYGNSS observations, R_{34} is estimated iteratively using a parametric wind model. This parametric 34-kt wind radius is denoted as $R_{34,P}$. The CYGNSS-IKE algorithm has two inputs: 1) the CYGNSS level 2 surface wind speed observations collected over a 3-h time period within a specified radius of the storm center and 2) the storm center location.

The interpolation of the wind field to points between those measured by CYGNSS takes advantage of the approximately symmetrical nature of hurricanes by using the parametric wind model based on Emanuel and Rotunno (2011):

$$v(r) = \frac{2r \left(R_m V_m + \frac{1}{2} f R_m^2 \right)}{R_m^2 + r^2} - \frac{fr}{2}, \quad (2)$$

where R_m is the radius of maximum winds, V_m is the maximum wind speed, r is the radial distance from

the storm center, and f is the Coriolis parameter. The Coriolis parameter is dependent on the storm center location coordinates. The model is illustrated in Fig. 2.

While there are many options of parametric wind model that could be used, the one chosen has been found to be especially amenable to use when fitting in a least squares sense to the CYGNSS samples, because it is continuous and has an analytical derivative. In addition, a study by Lin and Chavas (2012) finds that the model also has other desirable properties, when compared with other parametric wind models. There are some limitations to using Eq. (2), as discussed extensively in (Chavas et al. 2015): particularly, this model is most applicable to the region inwards of around $2.5R_m$. The simplicity of this model far outweighs the limitations.

The CYGNSS-IKE algorithm flow is illustrated in Fig. 3. The two free parameters of the model, R_m and V_m , are solved for using an iterative, least squares fit of the model to the CYGNSS observations. An example of the cost function to be minimized is shown in Fig. 4 as a function of R_m and V_m . The error surface is free of inflection points and the cost function has a single global minimum at the optimum (R_m, V_m) value. Such a well-behaved error surface makes the iterative algorithm

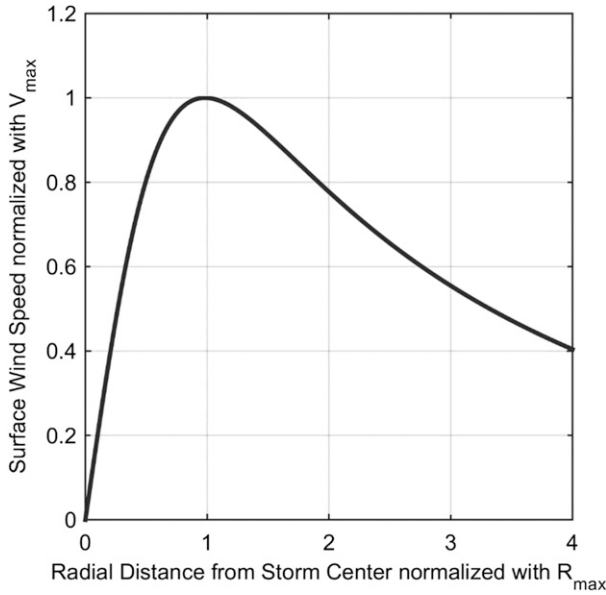


FIG. 2. A visualization of the parametric wind profile embedded within the CYGNSS-IKE algorithm. This model is described by Eq. (2), based on the work of Emanuel and Rotunno (2011) and recommended by Lin and Chavas (2012).

relatively insensitive to the first guess (which only affects the number of iterations required before convergence) and means a global minimum is generally found in each case.

The population of CYGNSS observations that are used in the parametric fit is all those samples lying within a distance R_{Limit} of the storm center. The value of R_{Limit} is initially set to 200 km. After the first iteration, the estimate of R_{34} given the parametric model, $R_{34,P}$, is compared with R_{Limit} . If they are not sufficiently close, then R_{Limit} is set equal to $R_{34,P}$, a new population of observations is selected, and the processes is repeated. Eventually (in practice within just a few iterations), the values of $R_{34,P}$ and R_{Limit} converge and the parametric-model estimation is complete.

The IKE is calculated from the parametric wind model by

$$IKE = \frac{\rho_0 \Delta z}{2} \int_0^{2\pi} \int_0^R v(\theta, r)^2 r dr d\theta, \quad (3)$$

where v is given by Eq. (2) and r is the radial distance from the storm center. The integration extends out to $R = R_{34,P}$, with an assumed Δz of 1 m, and a constant density ρ_0 of 1.15 kg m^{-3} —as suggested by Holland (1980).

4. Results

a. CYGNSS-IKE performance

The performance of the CYGNSS-IKE estimates is assessed by comparison with the true IKE derived by direct integration of the high-resolution HWRF wind fields. All 201 cases are considered. A portion of the 201 cases serve as test cases but do not meet the strength or observation criteria to compute IKE at the R_{34} threshold. There are two scenarios for which IKE is not estimated in a particular quadrant: 1) the quadrant was not observed by CYGNSS, or 2) CYGNSS did not observe winds that would have supported an estimate of R_{34} from the parametric-model fit. For example, if the quadrant wind field is well sampled by CYGNSS, but most of the wind speed estimates are lower than 34 kt, the parametric model trained to the observations will not predict, or support, winds over 34 kt. The performance statistics reported here are for comparisons when both HWRF and CYGNSS-based estimates of R_{34} IKE are possible. For the rest of the paper, unless otherwise noted, IKE refers to a quadrant-specific calculation of IKE.

First, as an example, Fig. 5 demonstrates IKE estimates possible over the course of the lifetime of one storm. Figure 5 shows the CYGNSS-IKE $_{R_{34,P}}$ and HWRF-IKE $_{R_{34}}$ values every 3 h throughout the life cycle of Hurricane Igor (2010) for instances of available simulated CYGNSS observations for all four storm quadrants. In general, the CYGNSS-IKE agrees closely

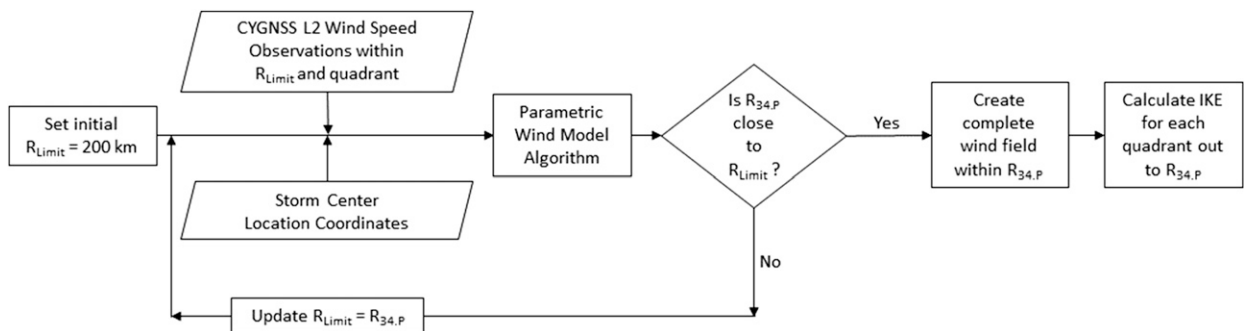


FIG. 3. A flowchart describing the steps within the CYGNSS-IKE algorithm.

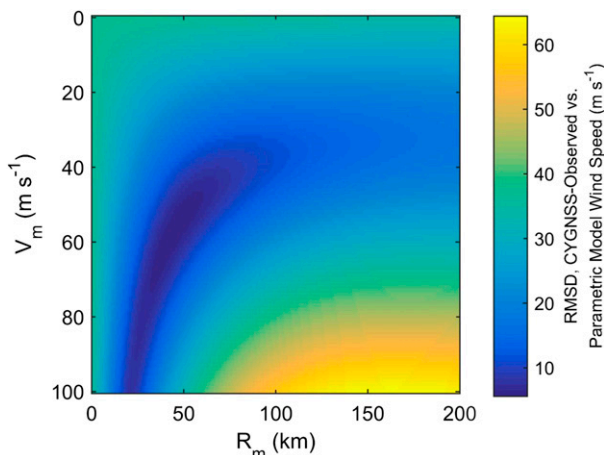


FIG. 4. An example of the cost function to be minimized, RMSD, is shown as a function of the parametric-model free variables, R_m and V_m from Eq. (2) for the Hurricane Igor test case at 1200 UTC 13 Sep 2010. For further reference and connection, Fig. 1 shows the HWRf wind field and corresponding CYGNSS observations that were input into the CYGNSS-IKE estimation process for this test case.

with the HWRf-IKE. However, Fig. 5 also highlights two main limitations of the current CYGNSS-IKE estimation process. At elapsed time 50 h, CYGNSS-IKE is not estimated for the NW and NE quadrants, while it was estimated from HWRf. In this case, CYGNSS did not have sufficient observations to support an estimate of R_{34} strength in the parametric model. Weaker case points sometimes miss the $R_{34,P}$ threshold—a requirement for IKE to be calculated in these methods—if they are not sampled sufficiently. A sufficient number of observations is required in a quadrant to accurately represent the wind field and support the parametric-model estimator. An example of the effects of sample size on performance can be seen in Fig. 5 in the southeast quadrant at 253 h, where CYGNSS-IKE is much less than HWRf-IKE. Outliers like this will be flagged based on CYGNSS coverage over a particular storm.

Figure 6 shows the overall performance of the CYGNSS-IKE estimate in comparison with HWRf-IKE. CYGNSS-IKE is estimated 412 times out of all 201 storm test cases. The two colors signify the quality control (QC) applied. Red dots indicate that the QC flag, developed in the following section, has been applied to that estimate.

b. Quality control threshold determination

To create estimates of IKE product trustworthiness, additional analysis was performed to create a QC flag for the CYGNSS-IKE estimate. Ideally, a QC flag would throw out as many outliers as possible, while still retaining the cases with good performance. Instinctively, one would expect sampling coverage by CYGNSS to

control the quality of the IKE estimate. A number of sampling thresholds were tested in combination to determine a practical CYGNSS-IKE QC flag. Figure 7 supports the decision making process for the ultimate QC flag choice. In the top subplot of Fig. 7, the IKE error is plotted with respect to two types of QC flags that are used in combination. IKE error is here defined as the normalized RMSD, with normalization of the difference between HWRf and CYGNSS-IKE by the HWRf-IKE being performed before the root-mean-square calculation.

To pass the QC test requires that

$$\text{num}_{\text{obs}} > N, \quad (4)$$

where num_{obs} is the number of observations over a storm quadrant and N is the minimum number of observations allowed, and that

$$\text{ratio}_s > S, \quad (5)$$

where ratio_s is the sampling ratio defined as

$$\text{ratio}_s = \frac{\text{num}_{\text{obs}}}{R_{34,P}} \quad (6)$$

in units of number per kilometer. The term S is the minimum sampling ratio required. On the Fig. 7 x axis, is ratio_s ; larger ratio_s correlates with better sampling over the extent of 34-kt winds. Each line in Fig. 7 shows the QC defined by Eq. (4), which only controls for the minimum number of observations needed for IKE estimation. Operated in combination, Eqs. (4) and (5) allow us to discard cases with poor sampling by CYGNSS. In general, the higher the threshold, the lower the error in the CYGNSS estimate. However, as noted in the bottom subplot of Fig. 7, the threshold also affects data coverage (i.e., fraction of remaining storm quadrant overpasses for which an IKE estimate is produced). The choice for the threshold should be an appropriate balance between data coverage and performance. We propose a QC flag that requires $N = 10$ observations and $S = 0.1$ observations per km; this threshold operates just above the “knee in the curve” with respect to performance and provides 88% data coverage.

The results of applying the chosen QC can be seen in Fig. 6, where red dots denote cases in which the flag is applied. Black dots show the cases that would remain after QC. The chosen QC flag gets rid of most of the outliers without a large loss of good cases.

c. Error decomposition

There are four main sources of error in the CYGNSS-IKE estimation. The first source results from the use of a

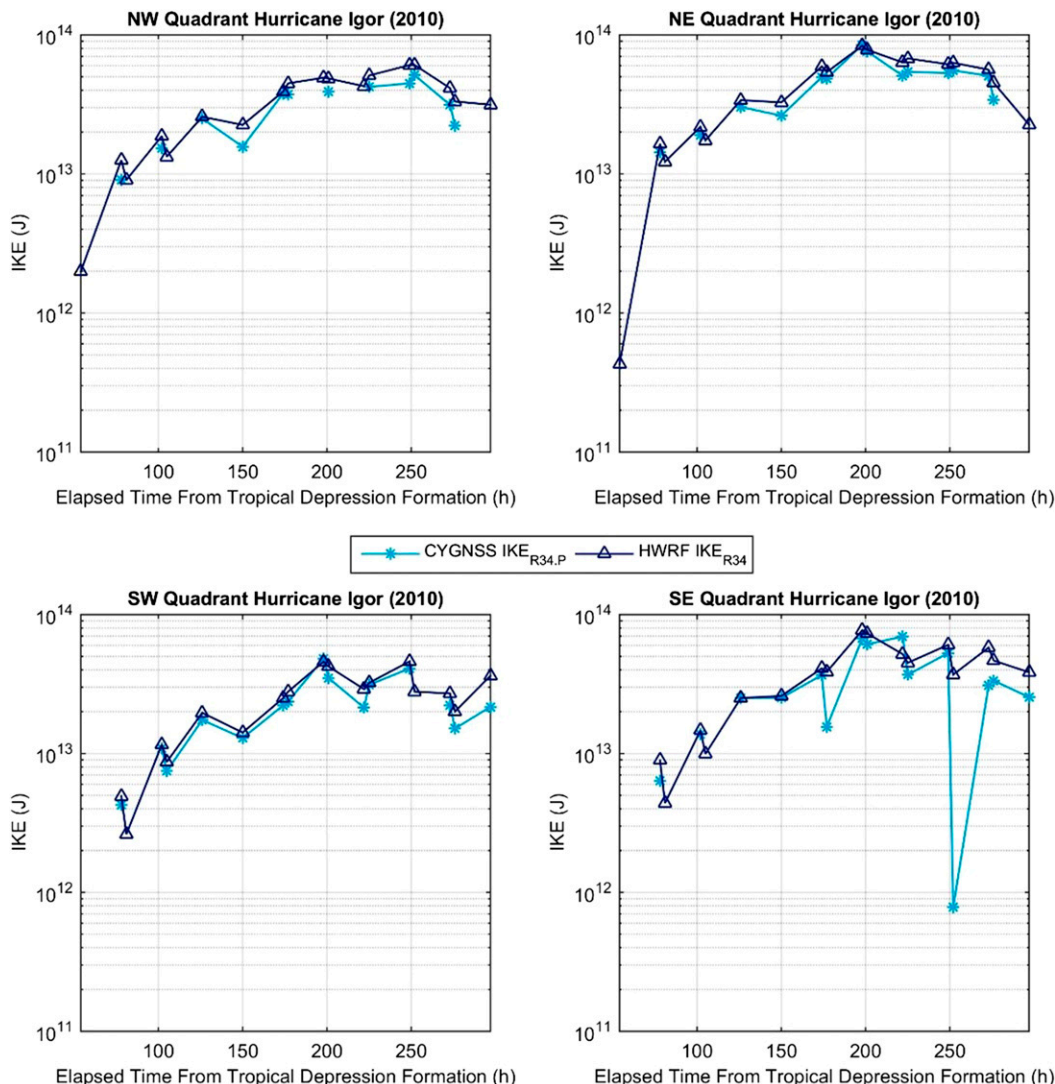


FIG. 5. A comparison of the IKE estimated from HWRf wind fields (truth) and simulated CYGNSS observations (retrieved) over the life cycle of Hurricane Igor (2010) as a function of the elapsed time since tropical depression formation at 0600 UTC 8 Sep 2010 (Pasch and Kimberlain 2011). For further reference and connection, Fig. 1 shows the HWRf wind field and corresponding CYGNSS observations that were initially input into the CYGNSS-IKE estimation process at elapsed time 126 h.

parametric wind model that is not representative of the true wind speed distribution. Second, CYGNSS sampling varies between 3-h intervals, with poorer coverage generally leading to worse estimates of IKE. Third, the CYGNSS wind speed measurements are not noise free, and the retrieval uncertainty will contribute to errors in the CYGNSS-IKE estimate. Fourth, imperfect knowledge of R_{34} will impact the performance of the algorithm because $R_{34,P}$ determines the population of observations used and defines the outer limit of integration of the IKE.

To compare the impact of these sources of errors, four experiments were run, each with a different type of wind speed input to the algorithm. The first experiment

assumes gap-free sampling of the wind field at the high-resolution HWRf reporting intervals. The samples are also assumed to be exact, with no CYGNSS measurement error. The parametric wind model is fit to these observations and then used to estimate IKE. Errors in the estimated IKE will in this case be due only to deviations of the true wind field from the parametric wind model.

The second experiment also assumes observations of the wind field without any CYGNSS measurement error, but now only at the locations at which CYGNSS would have sampled. In this case, errors in the estimated IKE will be due to both deviations from the ideal wind model and gaps in the wind observations. The third

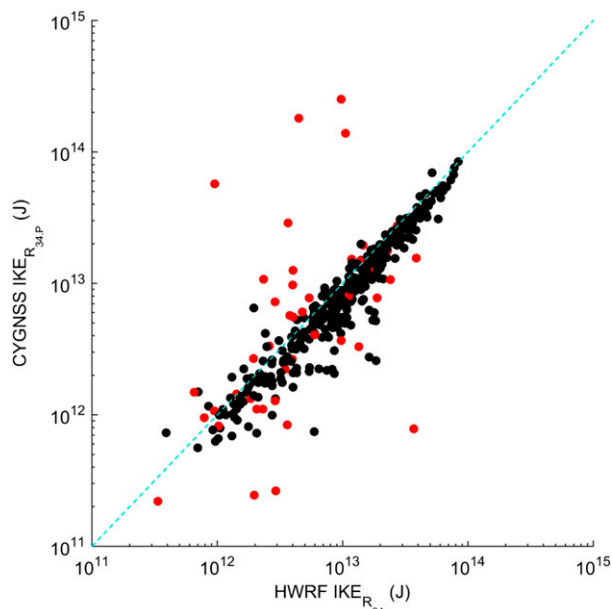


FIG. 6. A comparison of CYGNSS-IKE with the IKE estimated from HWRf for test cases defined from a set of simulated CYGNSS observations of Atlantic-basin and Pacific-basin storms occurring during 2010–11. Of 201 storm test cases, IKE is estimated for a particular quadrant 412 times. Red dots denote cases in which QC is flagged.

experiment is most realistic and assumes CYGNSS observations with realistic noise levels and at their appropriate sample locations. The fourth experiment is similar to the third experiment, but we assume perfect knowledge of R_{34} , which is calculated from HWRf for this analysis. Differences between the IKE calculated from these experiments and the HWRf-IKE allow for comparisons of the dominant error contributors to the CYGNSS-IKE estimation process.

Table 2 reports the results of these experiments. Overall, the CYGNSS-IKE performance is quite good, with 6.5% total unexplained variance due to all causes. The table also compares the percent unexplained variance that can be attributed to the individual sources of error. There is an increase in unexplained variance as the experiments include sparser and noisier wind fields. However, imperfect knowledge of R_{34} also impacts the performance of this estimation process. With perfect knowledge of R_{34} , the unexplained variance using true CYGNSS observations decreases from 6.5% to 3.9%, which is closest to the performance from the first, perfectly sampled, and noise-free experiment.

d. Storm center sensitivity

Since one of the inputs to the IKE algorithm is an estimate of the storm center location—which, for this study, comes from HWRf analyses—additional tests

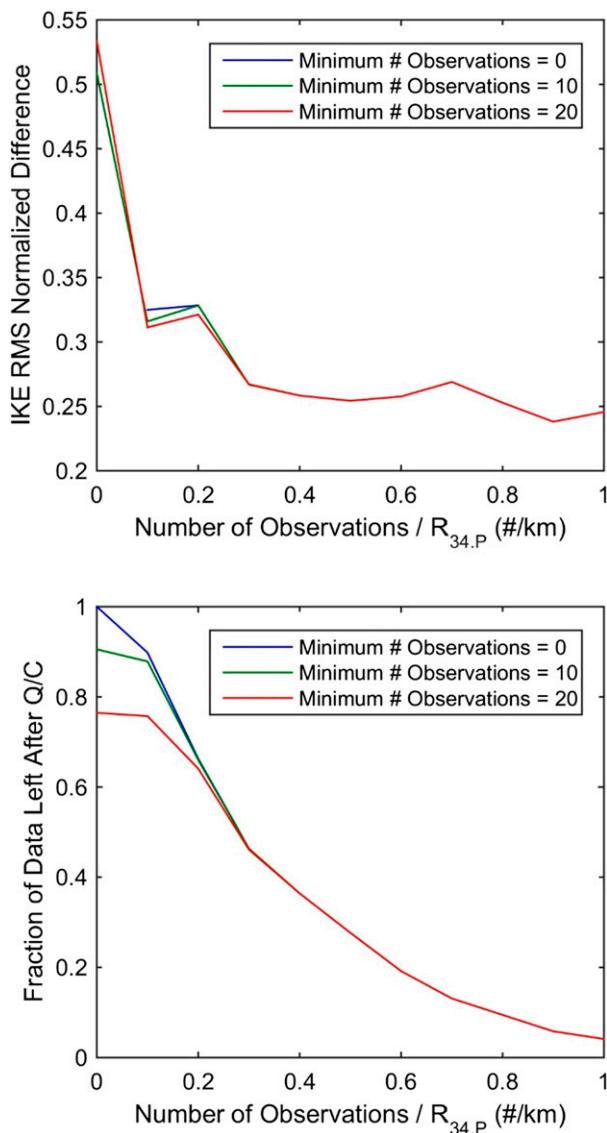


FIG. 7. (top) IKE RMS normalized difference between HWRf-IKE and CYGNSS-IKE with respect to two QC flags operated in combination. Each line represents the minimum number of observations allowed for a test case. Each line is plotted against a second QC flag, which controls for the ratio of the number of observations per the 34-kt wind radius in the parametric model ($R_{34,P}$). (bottom) Fraction of data left for all combinations of QC applied. The QC choice of >10 samples and >0.1 samples per kilometer leaves 88% of the test cases.

were performed to determine the sensitivity of the CYGNSS-IKE estimate to the accuracy of the storm center location. It is well known that the storm center is challenging to define for poorly organized storms. To test storm center location sensitivity, the coordinates were varied from the HWRf best estimate to locations $\pm 0.5^\circ$ in latitude. The CYGNSS observations were then reassembled according to the new (erroneous) storm

TABLE 2. Percent unexplained variance for experiments that used different input wind fields into the CYGNSS-IKE algorithm, where percent unexplained variance is $(1 - R^2) \times 100\%$.

Experiment input winds	Unexplained variance (%)
HWRP wind field	4.3
Noise-free CYGNSS wind speed observations	4.8
Noisy CYGNSS wind speed observations	6.5
Noisy CYGNSS wind speed observations with perfect $R_{\text{Limit}} = R_{34}$	3.9

center location. CYGNSS-IKE was found to be essentially insensitive to errors in storm center latitude within about 15 km north and south of the best estimate of storm center location. Outside of this range, the estimated IKE begins to degrade in accuracy. Center position uncertainty estimates vary widely depending on the strength of the storm, as well as the data available for position estimation (Torn and Snyder 2012; Landsea and Franklin 2013). For example, Torn and Snyder (2012) estimated position uncertainty to be around 37–65 km. While position uncertainty estimates from these studies are usually larger than 15 km, the authors hypothesize that the availability of CYGNSS data could be used to improve position estimates.

5. Discussion

Generally, the CYGNSS-IKE estimate is skillful. Performance depends most on the number of CYGNSS observations available for a given IKE estimate, which led to the formulation of a useful quality control flag. A CYGNSS-IKE estimate is generally more reliable as the number of samples increases. If a quality control flag is applied that limits estimates to cases with a minimum of 10 CYGNSS observations and a 0.1 sampling ratio, 88% of the coverage remains, the performance metrics improve, and the dominant source of IKE retrieval error is no longer the number of CYGNSS observations.

Other parameters were considered for use as a quality control parameter, but nothing else gave as much skill as the sample number flag. One potential parameter considered was the RMSD between the retrieved parametric wind model and the CYGNSS observations. However, the RMSD was found to be well correlated with the number of CYGNSS samples. With fewer samples, the RMSD of the parametric wind model fit tends to go down since it is generally easier to fit a model to fewer points. Thus, a low RMSD in this case does not mean the parametric wind model explains the wind field better, and so does not predict a better IKE estimate. An

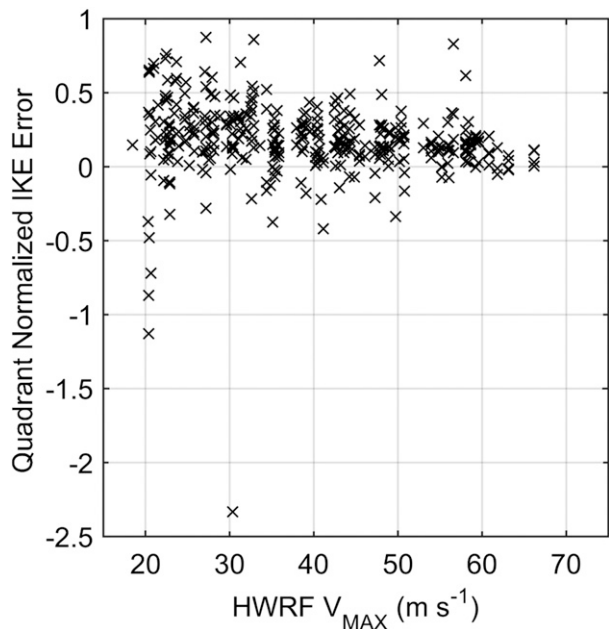


FIG. 8. The relative, quadrant-specific, IKE error of cases after QC with respect to the maximum wind speed found in the HWRP wind field. Quadrant normalized IKE error = $(\text{truth} - \text{estimated}) / \text{truth}$, where the truth here is derived from HWRP.

accurate IKE estimate requires the wind field to be well sampled, not that the RMSD in the parametric model be low.

Generally, the CYGNSS-IKE estimate performs better in intense storms because the parametric wind model is more applicable in these cases—stronger storms tend to be better organized and hence correspond more closely to the parametric model. Figures 8 and 9 summarize the relationship between relative IKE error and maximum wind speed (V_{MAX}). Figure 8 compares data for quadrant-IKE, while Fig. 9 shows the results from total (sum over all quadrants) IKE. In Fig. 9, only cases where estimates of IKE were available for all four quadrants are considered. Figure 8 shows that the large outliers in quadrant-IKE performance occur more often in cases with low V_{MAX} ; many of the low-intensity outliers result from large overestimates of the IKE. Aside from the outliers at low V_{MAX} , CYGNSS-IKE performs relatively consistently across the range of intensity. Figure 9 shows the results if considering total-IKE over the entire storm. Performance improves for these cases relative to the results in Fig. 8. Improvements from quadrant-IKE to total-IKE are likely due to two main things. First, comparisons of total-IKE are only made for cases in which all four quadrants have IKE estimates. Second, quadrant-IKE errors will partially cancel out after summation.

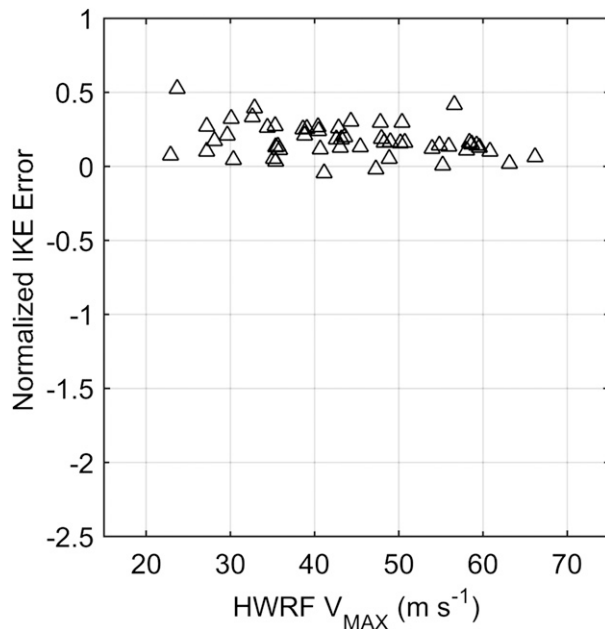


FIG. 9. The relative IKE error of cases after QC, with respect to the maximum wind speed found in the HWRf wind field. Normalized IKE error = (truth – estimated)/truth, where the truth here is derived from HWRf. IKE is summed over all quadrants for cases in which there were estimates of IKE for all quadrants available.

Overall, Figs. 8 and 9 show there is a low bias in the CYGNSS-IKE, regardless of whether it is a total or quadrant-specific value. The bias in CYGNSS-IKE is likely due to the fact that we are training the parametric model to the CYGNSS observations in a best-fit sense to estimate the full wind field. CYGNSS-IKE is calculated out to the radial extent of the 34-kt winds in the parametric model, rather than the true extent. Future work will include analyzing this bias further on a wider range of cases, as well as determining solutions to correct it.

6. Conclusions

CYGNSS will provide the opportunity to observe tropical cyclones (TCs) with unprecedented temporal and spatial sampling. With this new observing system come challenges and questions to be explored. In this paper we consider how well IKE can be estimated from its observations.

With applications ranging from storm surge prediction to situational awareness, users of the CYGNSS-IKE product could include operational and research meteorologists, insurance companies, and anyone interested in TCs generated in data-sparse, but CYGNSS-covered, regions. IKE is particularly useful considering it is often more correlated with storm surge at TC landfall than is the V_{MAX} or intensity of the storm.

Future work includes investigating ways of improving these methods, especially postlaunch with CYGNSS observations. Additionally, the parametric wind model algorithm has several potential applications outside of IKE estimation. A variety of useful parameters—intensity and wind radii—could be derived using the parametric wind model algorithm and CYGNSS data.

Acknowledgments. The authors thank the reviewers for their in-depth reviews and helpful suggestions that have helped to improve this paper. The authors acknowledge the hard work of several CYGNSS science team members that supported this work. The HWRf dataset was gathered by Faozi Said and Golf Seubson Soisuvann. The simulated CYGNSS observations were developed based on the work by Andrew O'Brien and Aaron Ridley. This work was supported in part by NASA Science Mission Directorate Contract NNL13AQ00C.

REFERENCES

- Bessho, K., M. DeMaria, and J. A. Knaff, 2006: Tropical cyclone wind retrievals from the Advanced Microwave Sounding Unit (AMSU): Application to surface wind analysis. *J. Appl. Meteor. Climatol.*, **45**, 399–415, doi:10.1175/JAM2352.1.
- Brennan, M. J., C. C. Hennon, and R. D. Knabb, 2009: The operational use of QuikSCAT ocean vector winds at the National Hurricane Center. *Wea. Forecasting*, **24**, 621–645, doi:10.1175/2008WAF2222188.1.
- Chavas, D. R., N. Lin, and K. Emanuel, 2015: A model for the complete radial structure of the tropical cyclone wind field. Part I: Comparison with observed structure. *J. Atmos. Sci.*, **72**, 3647–3662, doi:10.1175/JAS-D-15-0014.1.
- Clarizia, M. P., and C. S. Ruf, 2016: Wind speed retrieval algorithm for the Cyclone Global Navigation Satellite System (CYGNSS) mission. *IEEE Trans. Geosci. Remote Sens.*, **54**, 4419–4432, doi:10.1109/TGRS.2016.2541343.
- Dunion, J. P., and C. S. Velden, 2002: Application of surface-adjusted GOES low-level cloud-drift winds in the environment of Atlantic tropical cyclones. Part I: Methodology and validation. *Mon. Wea. Rev.*, **130**, 1333–1346, doi:10.1175/1520-0493(2002)130<1333:AOSAGL>2.0.CO;2.
- Emanuel, K., and R. Rotunno, 2011: Self-stratification of tropical cyclone outflow. Part I: Implications for storm structure. *J. Atmos. Sci.*, **68**, 2236–2249, doi:10.1175/JAS-D-10-05024.1.
- Hennon, C. C., D. Long, and F. Wentz, 2006: Validation of QuikSCAT wind retrievals in tropical cyclone environments. Preprints, *14th Conf. on Satellite Meteorology and Oceanography*, Atlanta, GA, Amer. Meteor. Soc., JP1.1. [Available online at <http://ams.confex.com/ams/pdfpapers/99478.pdf>.]
- Holland, G. J., 1980: An analytic model of the wind and pressure profiles in hurricanes. *Mon. Wea. Rev.*, **108**, 1212–1218, doi:10.1175/1520-0493(1980)108<1212:AAMOTW>2.0.CO;2.
- Holmlund, K., C. Velden, and M. Rohn, 2001: Enhanced automated quality control applied to high-density satellite-derived winds. *Mon. Wea. Rev.*, **129**, 517–529, doi:10.1175/1520-0493(2001)129<0517:EAQCAT>2.0.CO;2.

- Irish, J. L., D. T. Resio, and J. J. Ratcliffe, 2008: The influence of storm size on hurricane surge. *J. Phys. Oceanogr.*, **38**, 2003–2013, doi:10.1175/2008JPO3727.1.
- Kantha, L., 2006: Time to replace the Saffir–Simpson hurricane scale? *Eos, Trans. Amer. Geophys. Union*, **87**, 3–6, doi:10.1029/2006EO010003.
- Kieper, M. E., C. W. Landsea, and J. L. Beven, 2016: A reanalysis of Hurricane Camille. *Bull. Amer. Meteor. Soc.*, **97**, 367–384, doi:10.1175/BAMS-D-14-00137.1.
- Knabb, R. D., J. R. Rhome, and D. P. Brown, 2005: Tropical cyclone report: Hurricane Katrina. NOAA/NHC, 43 pp. [Available online at http://www.nhc.noaa.gov/data/tcr/AL122005_Katrina.pdf.]
- Knaff, J. A., M. DeMaria, D. A. Molenaar, C. R. Sampson, and M. G. Seybold, 2011: An automated, objective, multisatellite platform tropical cyclone surface wind analysis. *J. Appl. Meteor. Climatol.*, **50**, 2149–2166, doi:10.1175/2011JAMC2673.1.
- , S. P. Longmore, R. T. DeMaria, and D. A. Molenaar, 2015: Improved tropical-cyclone flight-level wind estimates using routine infrared satellite reconnaissance. *J. Appl. Meteor. Climatol.*, **54**, 463–478, doi:10.1175/JAMC-D-14-0112.1.
- Kossin, J. P., J. A. Knaff, H. I. Berger, D. C. Herndon, T. A. Cram, C. S. Velden, R. J. Murnane, and J. D. Hawkins, 2007: Estimating hurricane wind structure in the absence of aircraft reconnaissance. *Wea. Forecasting*, **22**, 89–101, doi:10.1175/WAF985.1.
- Kozar, M. E., 2015: Analysis and prediction of integrated kinetic energy in Atlantic tropical cyclones. Ph.D. dissertation, Florida State University, 197 pp. [Available online at http://purl.flvc.org/fsu/fd/FSU_migr_etd-9376.]
- , and V. Misra, 2014: Statistical prediction of integrated kinetic energy in North Atlantic tropical cyclones. *Mon. Wea. Rev.*, **142**, 4646–4657, doi:10.1175/MWR-D-14-00117.1.
- , —, and M. Powell, 2016: Hindcasts of integrated kinetic energy in Atlantic tropical cyclones: A neural network prediction scheme. *Mon. Wea. Rev.*, **144**, 4591–4603, doi:10.1175/MWR-D-16-0030.1.
- Landsea, C. W., and J. L. Franklin, 2013: Atlantic hurricane database uncertainty and presentation of a new database format. *Mon. Wea. Rev.*, **141**, 3576–3592, doi:10.1175/MWR-D-12-00254.1.
- Lin, N., and D. Chavas, 2012: On hurricane parametric wind and applications in storm surge modeling. *J. Geophys. Res.*, **117**, D09120, doi:10.1029/2011JD017126.
- Maclay, K. S., M. DeMaria, and T. H. Vonder Haar, 2008: Tropical cyclone inner-core kinetic energy evolution. *Mon. Wea. Rev.*, **136**, 4882–4898, doi:10.1175/2008MWR2268.1.
- Mahendran, M., 1998: Cyclone intensity categories. *Wea. Forecasting*, **13**, 878–883, doi:10.1175/1520-0434(1998)013<0878:CIC>2.0.CO;2.
- Misra, V., S. DiNapoli, and M. Powell, 2013: The track integrated kinetic energy of Atlantic tropical cyclones. *Mon. Wea. Rev.*, **141**, 2383–2389, doi:10.1175/MWR-D-12-00349.1.
- Mueller, K. J., M. DeMaria, J. A. Knaff, J. P. Kossin, and T. H. Vonder Haar, 2006: Objective estimation of tropical cyclone wind structure from infrared satellite data. *Wea. Forecasting*, **21**, 990–1005, doi:10.1175/WAF955.1.
- NOAA/NESDIS/STAR/RAMMB, 2016: Real-time tropical cyclone products—Description of products. Accessed 9 May 2016. [Available online at http://rammb.cira.colostate.edu/products/tc_realtime/about.asp.]
- O'Brien, A., 2014: Cyclone Global Navigation Satellite System (CYGNSS) end-to-end simulator. CYGNSS Project Doc. 148-0123, 24 pp. [Available online at http://clasp-research.engin.umich.edu/missions/cygnss/reference/148-0123_CYGNSS_E2ES_EM.pdf.]
- Pasch, R. J., and T. B. Kimberlain, 2011: Tropical cyclone report: Hurricane Igor. NOAA/NHC, 20 pp. [Available online at http://www.nhc.noaa.gov/data/tcr/AL112010_Igor.pdf.]
- Powell, M. D., and T. A. Reinhold, 2007: Tropical cyclone destructive potential by integrated kinetic energy. *Bull. Amer. Meteor. Soc.*, **88**, 513–526, doi:10.1175/BAMS-88-4-513.
- , S. H. Houston, L. R. Amat, and N. Morisseau-Leroy, 1998: The HRD real-time hurricane wind analysis system. *J. Wind Eng. Ind. Aerodyn.*, **77–78**, 53–64.
- , and Coauthors, 2010: Reconstruction of Hurricane Katrina's wind fields for storm surge and wave hindcasting. *Ocean Eng.*, **37**, 26–36, doi:10.1016/j.oceaneng.2009.08.014.
- Ruf, C. S., and Coauthors, 2016: New ocean winds satellite mission to probe hurricanes and tropical convection. *Bull. Amer. Meteor. Soc.*, **97**, 385–395, doi:10.1175/BAMS-D-14-00218.1.
- Saffir, H., 1975: Low-cost construction resistant to earthquakes and hurricanes. United Nations ST/ESA/23, 205 pp.
- Simpson, R. H., 1974: The hurricane disaster-potential scale. *Weatherwise*, **27**, 169–186, doi:10.1080/00431672.1974.9931702.
- Tallapragada, V., and Coauthors, 2013: Hurricane Weather Research and Forecasting (HWRF) Model: 2013. DTC, 99 pp. [Available online at http://www.dtcenter.org/HurrWRF/users/docs/scientific_documents/HWRFv3.5a_ScientificDoc.pdf.]
- Torn, R. D., and C. Snyder, 2012: Uncertainty of tropical cyclone best-track information. *Wea. Forecasting*, **27**, 715–729, doi:10.1175/WAF-D-11-00085.1.
- Velden, C. S., C. M. Hayden, S. J. Nieman, W. P. Menzel, S. Wanzong, and J. S. Goerss, 1997: Upper-tropospheric winds derived from geostationary satellite water vapor observations. *Bull. Amer. Meteor. Soc.*, **78**, 173–195, doi:10.1175/1520-0477(1997)078<0173:UTWDFG>2.0.CO;2.
- , and Coauthors, 2005: Recent innovations in deriving tropospheric winds from meteorological satellites. *Bull. Amer. Meteor. Soc.*, **86**, 205–223, doi:10.1175/BAMS-86-2-205.